Surface and Interfacial Engineering of Iron Oxide Nanoplates for Highly Efficient Magnetic Resonance Angiography

Zijian Zhou,[†,§] Changqiang Wu,[‡,§] Hanyu Liu,[†] Xianglong Zhu,[†] Zhenghuan Zhao,[†] Lirong Wang,[†] Ye Xu,[‡] Hua Ai,[‡] and Jinhao Gao*[,†]

[†]State Key Laboratory of Physical Chemistry of Solid Surfaces, The Key Laboratory for Chemical Biology of Fujian Province, and Department of Chemical Biology, College of Chemistry and Chemical Engineering, Xiamen University, Xiamen 361005, China and [‡]National Engineering Research Center for Biomaterials, and Department of Radiology, West China Hospital, Sichuan University, Chengdu 610064, China. [§]Z.Z. and C.W. contributed equally to this work.

ABSTRACT Magnetic resonance angiography using gadolinium-based molecular contrast agents suffers from short diagnostic window, relatively low resolution and risk of toxicity. Taking into account the chemical exchange between metal centers and surrounding protons, magnetic nanoparticles with suitable surface and interfacial features may serve as alternative T_1 contrast agents. Herein, we report the engineering on surface structure of iron oxide nanoplates to boost T_1 contrast ability through synergistic effects between exposed metal-rich $Fe_3O_4(100)$ facets and embedded Gd_2O_3 clusters. The nanoplates show prominent T_1 contrast in a wide range of magnetic fields with an ultrahigh r_1 value up to 61.5 mM^{-1} s^{-1}. Moreover, engineering on nanobio interface through zwitterionic molecules adjusts the *in vivo* behaviors of nanoplates for highly efficient magnetic resonance angiography with steady-state acquisition window, superhigh resolution in vascular details, and low toxicity. This study provides a powerful tool for sophisticated design of MRI contrast agents for diverse use in bioimaging applications.

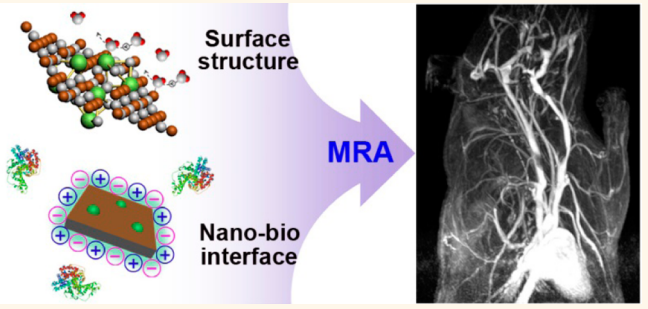

KEYWORDS: blood pool contrast agents · surface structure · interface · MRA · high-performance

Magnetic resonance imaging (MRI) is a noninvasive and tomographic technique with high spatial resolution in tissue contrast, which holds great promise for disease diagnosis in clinic.[1] Approximately 35% of clinical MR scans are aided with contrast agents to improve diagnostic accuracy.[2,3] Because of good biocompatibility and excellent magnetic properties,[4,5] iron oxide nanoparticles have been extensively explored as MRI contrast agents through controlling over the size,[6−9] composition,[10−12] and morphology.[13−15] For example, iron oxide nanoparticles show feasible T_1 contrast by decreasing the size to approximately 3 nm, which were employed as magnetic resonance angiography (MRA) contrast agents.[7] Contrast-enhanced MRA is an established clinical tool enabling to detect and evaluate a variety of vascular pathologies.[16−18] However, ultrasmall iron oxide nanoparticles cannot output high-level diagnostic information about vascular details (*e.g.*, veins) in MRA due to the relatively low T_1 contrast ability and intrinsic T_2 interference. Gadolinium chelating molecules are employed as diagnostic T_1 contrast agents in clinic; however, these molecular contrast agents suffer from poor physiological stability, uncontrollable pharmacokinetics, and a risk of toxicity.[19−21] MRA studies using conventional molecular agents are also limited by short acquisition windows due to the rapid perfusion of molecules into extracellular compartments after first pass of aorta.[22] Development of novel contrast agents that overcome low efficiency and poor biodistribution are urgently needed for highly efficient MRA.

* Address correspondence to jhgao@xmu.edu.cn.

Received for review December 17, 2014 and accepted February 10, 2015.

Published online February 11, 2015
10.1021/nn507193f

Surface and interfacial properties of nanoparticles play an important role in their interactions with surroundings, such as protons and biological media during *in vivo* studies.[23,24] Recently, we demonstrated that exposed metals on the surface of magnetite nanoplates are major contributions to protons T_1 relaxation enhancement because of the sufficient magnetic centers for protons coordination and chemical exchange.[25] The magnetite nanoplates with iron-rich (111) exposed surfaces also have tunable T_1 relaxivities through regulating (111) surface-to-volume ratio of nanoplates. However, iron ions show relatively low contrast ability in T_1 imaging, especially in higher magnetic fields (*e.g.*, clinical 3.0 T), which limits the use of nanoplates for bioimaging applications. The nanobio interface between nanoparticles and biological media is another key factor that may determine the biological identity and eventually, influence the *in vivo* behaviors of nanoparticles.[26,27] Foreign nanoparticles are prone to being recognized by immune systems and accumulating in liver and spleen, leading to uncontrollable distributions and unexpected pharmaceutical effects *in vivo*. Therefore, a suitable surface functionality of nanoparticles is extremely important to regulate the nanobio interface for desirable utility in complex biological systems.

Herein, we present novel engineered iron oxide nanoplates, which is composed of exposed Fe_3O_4(100) facets and embedded Gd_2O_3 clusters, as a highly efficient T_1 contrast agent for high-resolution MRA in small animals. The T_1 relaxivity of Gd_2O_3-embedded iron oxide nanoplates (GdIOPs) was greatly enhanced due to a large proportion of exposed metals (*i.e.*, Fe and Gd) on surface. Moreover, we successfully regulated the *in vivo* behaviors of GdIOP through engineering the nanobio interface using different functional molecules. GdIOP with protein corona can serve as an efficient T_1-T_2 dual-modal contrast agent for accurate imaging of liver and detection of liver lesions. Corona-free GdIOP with ultrahigh T_1 relaxivity can achieve high-resolution MRA with a prolonged acquisition window and low potential of gadolinium-induced toxicity comparing to the commerical agent Magnevist. The engineered GdIOPs have a great potential to act as highly efficient MRI contrast agents for imaging and diagnosis of cancer and cardiovascular diseases.

RESULTS AND DISCUSSION

Synthesis and Characterization. We synthesized the GdIOPs by thermal decomposition of gadolinium oleate and iron oleate complexes in 1-octadecene, as well as the presence of oleic acid as surfactant (detailed in the Methods). The X-ray photoelectron spectroscopy (XPS) analysis of the obtained GdIOPs reveals typical magnetite phase with the peaks at 711.4 and 724.2 eV coresponding to Fe 2p3/2 and Fe 2p1/2 transitions,[28,29] respectively (Figure S1 in Supporting Information). Representative transmission electron microscopy (TEM) images show the nanoplates are uniform with length of about 9 nm (Figure 1a, and Figure S2 in Supporting Information). In the high-resolution TEM (HRTEM) image of a flatten nanoplate, a pair of perpendicular crossed Fe_3O_4(220) planes with the interplanar spacing distance of 3.1 Å indicates that the planar surface of nanoplates are exposed with (100) facets (Figure 1b). We also notice that they are in shape of nanoplates with a thickness of about 1.8 nm (Figure 1c), rather than cubes. HRTEM image of a vertical nanoplate further shows that the nanoplates are with only three-layer periodicity of atomic arrangement of Fe_3O_4(100) planes, in which the interplanar spacing distance is 8.4 Å (Figure 1c, inset). On the basis of these findings, we propose that the obtained nanoplates are packed with only two cells of Fe_3O_4 crystal in thickness, which is rarely reported previously. The X-ray diffraction (XRD) pattern of GdIOP indicates that there are mixed magnetite (JCPDS. 65−3107) and Gd_2O_3 (JCPDS. 012−0474) phases, which is consistent with the select-area electron diffraction (SAED) pattern (Figure S3 in Supporting Information). This result implies a domain-aggregated structure of GdIOP composed of Gd_2O_3 clusters and Fe_3O_4 domains. The presence of Gd species were also confirmed by energy-dispersive X-ray (EDX) element mapping and line scanning analysis, exhibiting homogeneous distributions of Gd and Fe elements across nanoplates (Figure 1d,e). The molar percentage of Gd with respect to total metals is about 14.2% measured by inductively coupled plasma atomic emission spectroscopy (ICP-AES) analysis.

We also used synchrotron X-ray absorption spectroscopy (XAS) to further envision the structure of GdIOP. XAS spectrum of GdIOP shows an additional peak at about 7248 eV comparing to that of single-domain Fe_3O_4 nanoparticles (Figure 1f). This peak is attributed to overlap of Fe K-edge fluctuations and Gd L_{III}-edge absorption. The X-ray absorption near edge structure (XANES) spectrum is a sensitive method to analyze coordination geometry, bonding environment, and electronic structure of central atoms.[30] The Fe K-edge XANES spectrum of GdIOP shows a white-line peak at 7130 eV, similar to that of Fe_3O_4 sample (Figure 1g). In addition, a pre-edge peak at 7112.5 eV can be found in both GdIOP and Fe_3O_4 samples, which is ascribed to 1s → 3d (quadrupolar) and 1s → 4p (dipolar) electronic transitions of tetrahedral and octahedral iron ions.[30] The decreased adsorption intensity may be attributed to increased structural disorder in GdIOP comparing to that of Fe_3O_4 sample,[31] which further confirms that long-range-order of iron oxide domains in GdIOP may be perturbed by the existence of Gd_2O_3 clusters.

Field-dependent magnetization ($M-H$) curves of GdIOP show saturation magnetization moments (M_s)

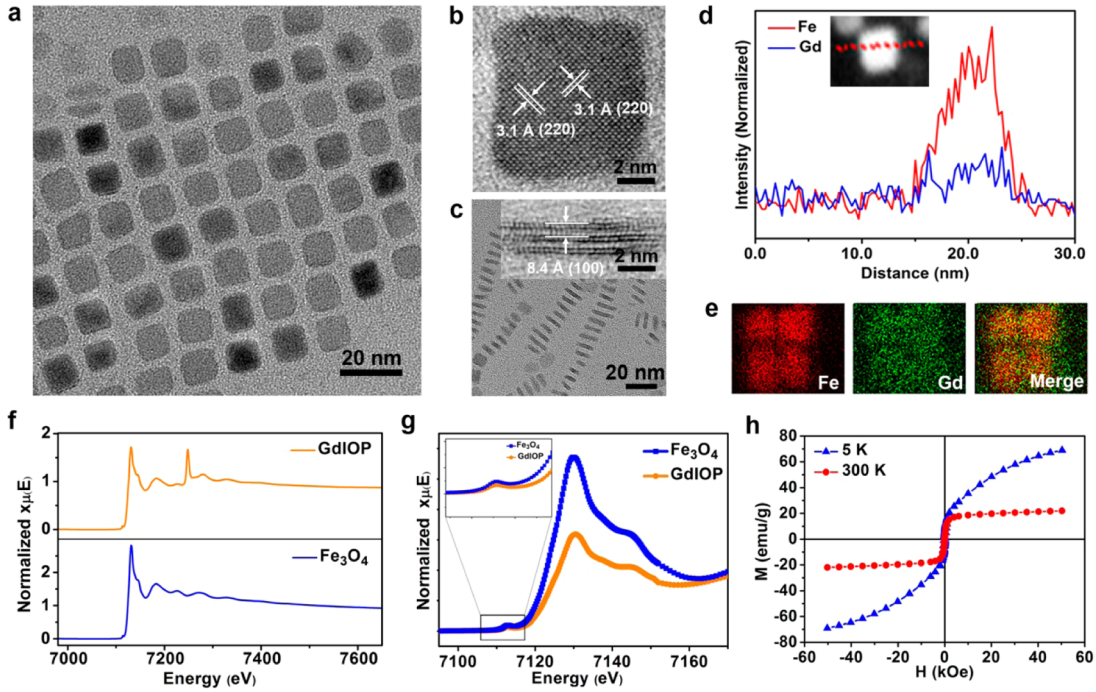

Figure 1. Characterizations of GdIOP. (a,b) TEM and HRTEM images of on-plane view of GdIOP, respectively, showing Fe_3O_4(100) basal planes of GdIOP. (c) TEM and HRTEM (inset) images of vertically aligned GdIOP, indicating three-layer periodicity of Fe_3O_4(100) planes (each with about 8.4 Å) in thickness. (d) EDX line-scanning features across a GdIOP (inset) and (e) elemental mapping images, showing uniformly distributed Gd and Fe elements. (f) Normalized Fe K-edge XAS spectrum of GdIOP and Fe_3O_4 (single-domain) samples using transmittance mode. (g) Fe K-edge XANES spectrum of GdIOP and Fe_3O_4 samples. The reduced intensity of GdIOP indicates the increased structural disorder comparing to that of Fe_3O_4 samples. (h) *M*−*H* curves at 300 and 5 K show partially paramagnetism due to the domain-aggregated structure of GdIOP.

are about 21.9 and 68.8 emu/g at 300 and 5 K (Figure 1h), respectively. The *M*−*H* curves of GdIOP also show partially paramagnetism probably due to the presence of Gd_2O_3 clusters. Zero-field cooling (ZFC) and field cooling (FC) measurements give the blocking temperature (T_B) of GdIOP at about 90 K (Figure S4 in Supporting Information). GdIOPs reveal a remarkable M_s deviation (~46.9 emu/g) between 300 and 5 K, which is significantly different from those of superparamgnetic single-domain Fe_3O_4 nanoparticles, usually with deviation less than 10 emu/g. This phenomenon may be attributed to the high level of long-range-order disturbance at 300 K because thermal agitation effect is enhanced by the existence of multiple domains in GdIOP. On the contrary, at low temperature (5 K) below T_B, thermal agitation effect becomes less dominated so that spin reorientation occurs and leads to much higher magnetic moments. These results indicate that GdIOP is composed of Fe_3O_4(100) facets exposed iron oxide domains and Gd_2O_3 clusters, which may have great potential in T_1 and T_2 relaxation enhancements.

Surface Structure and MRI Performance. We then studied the contrast enhancement ability by MR phantom with different concentrations of GdIOP, which can provide intuitional views of contrast ability by distinguishing brightness (T_1) or darkness (T_2) of the images. The GdIOP samples with different concentrations (with respect to total metal ions) were prepared and conducted with both T_1- and T_2-weighted MRI study under four different magnetic fields (0.5, 3.0, 7.0, and 9.4 T). The GdIOPs show clear contrast in T_1-weighted imaging at 0.5, 3.0, and 7.0 T MRI scanners (Figure 2a), while the weak T_1 contrast at 9.4 T may be due to strong T_2 interference in such a high magnetic field. T_2 contrasts of GdIOP are evident in all magnetic fields, indicating an intrinsic transverse decaying effect of iron oxide domains (Figure 2a).

The relaxivity results show that GdIOP owes a large r_1 value of 61.5 ± 3.1 mM^{-1} s^{-1} (the mM represents to the concentration of total metal (Fe + Gd) ions) at 0.5 T. Then the r_1 value decreases to 20.5 ± 0.5, 6.8 ± 1.3, and 4.3 ± 0.7 mM^{-1} s^{-1} as elevating applied fields to 3.0, 7.0, and 9.4 T, respectively (Table 1). The enhanced T_1 relaxivity of GdIOP can be attributed to both iron-terminated Fe_3O_4(100) basal planes and the exposed Gd_2O_3 clusters (Figure 2b). Exposed Fe and Gd ions may synergistically enhance protons T_1 relaxation by providing efficient paramagnetic islands for protons coordination and chemical exchange. Besides, protons T_1 relaxation would also benefit from convenient hopping on the flatten surface of GdIOP, which may further interact with nearby metals in one relaxation process.[32,33] To further confirm these hypothesis, we prepared spherical GdIO nanoparticles and Fe_3O_4(100) facets enclosed IO nanocubes. The spherical GdIO nanoparticles are about 12 nm in diameter with Gd percentages of about 13.8%, and the IO cubes are

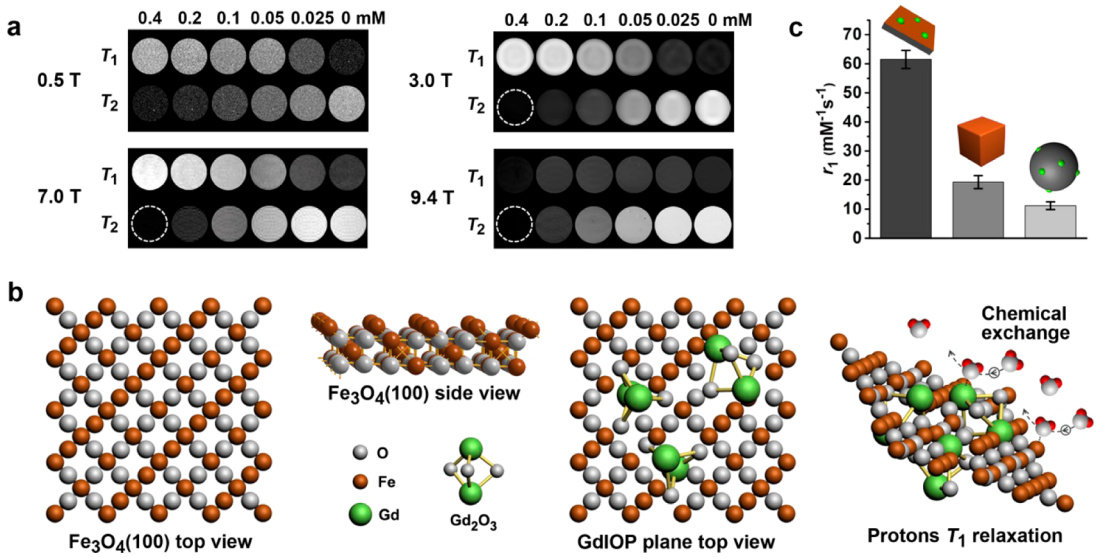

Figure 2. Surface structure and MRI performance. (a) T_1- and T_2-weighted phantom imaging of GdIOPs under four different magnetic fields (0.5, 3.0, 7.0, and 9.4 T), suggesting good contrasts in T_1-T_2 dual-modal imaging in a wide range of magnetic field (0.5, 3.0, and 7.0 T). At 9.4 T, GdIOPs mainly show T_2-dominated contrast ability. (b) Atomic top and side views of Fe_3O_4(100) basal planes and Gd_2O_3 decorated surface characteristics of GdIOP. The exposed iron and gadolinium ions on the surface of GdIOPs may provide efficient chemical exchange for protons, accelerating the T_1 relaxation. The sizes of atoms are not to scale. (c) Comparison of r_1 values of GdIOPs, IO cubes, and GdIO spheres in 0.5 T (n = 3. Data represent mean ± s.d.). The IO cubes are packed with six Fe_3O_4(100) planes but without Gd species, GdIO spheres are with similar Gd doping but without metal-rich Fe_3O_4(100) planes.

TABLE 1. r_1 and r_2 Values of GdIOPs under Different Magnetic Fields[a]

H_0 (T)	r_1 (mM^{-1} s^{-1})	r_2 (mM^{-1} s^{-1})	r_2/r_1
0.5	61.5 ± 3.1	147.2 ± 3.7	2.4
3.0	20.5 ± 0.5	145.4 ± 11.5	7.1
7.0	6.8 ± 1.3	158.8 ± 5.4	23.4
9.4	4.3 ± 0.7	167.6 ± 7.2	38.9

[a] The mM represents to concentrations of total iron and gadolinium ions (n = 3. Data represent mean ± s.d.).

about 15 nm in side lengths enclosed by six Fe_3O_4(100) facets (Figure S5 in Supporting Information). Under the same conditions at 0.5 T, the r_1 values are 11.2 and 19.3 mM^{-1} s^{-1} for the spherical GdIO and the cubic IO nanoparticles, respectively, much lower than that of GdIOP (Figure 2c). These results indicate that T_1 relaxation enhancement of GdIOP is contributed to both paramagnetic clusters and surface exposed iron ions.

T_2 relaxation enhancement is related to proton spin−spin relaxation turbulence by local field inhomogeneity, therefore, nonspherical nanostructures (*e.g.*, cubes, octapods) possessing large-area effective region were recognized as enhanced T_2 contrast agents.[13,15] Additionally, r_2 value is also proportional to M_s on the basis of outersphere theory that laid the foundations for general knowledge of magnetic contrast agents.[34,35] Thus, r_2 value of GdIOP may be influenced by three factors: (i) M_s, (ii) effective radii, and (iii) synergistic effects between nanoscale iron oxide domains, which may achieve a larger r_2 value than that of individuals.[36,37] As a result, GdIOPs exhibit a relatively large r_2 value of 147.2 ± 3.7 mM^{-1} s^{-1} at 0.5 T, even the M_s is as low as 21.9 emu/g at 300 K. It is interesting that the r_2 value increased moderately to 145.4 ± 11.5, 158.8 ± 5.4, and 167.6 ± 7.2 mM^{-1} s^{-1} at 3.0, 7.0, and 9.4 T, respectively (Table 1). This phenomenon is different from that of superparamagnetic nanoparticles, which usually show dramatically increased r_2 values as elevating magnetic fields due to the high M_s. One major obstacle for superparamagnetic nanoparticles to exhibit T_1 contrast ability at higher fields (*e.g.*, clinical 3.0 T) is the strong T_2 decaying effect at transverse direction, which reduces T_1 signal recovery when it rolls from longitudinal to trasnverse direction in principle.[1] Therefore, the fabrication of domain-bounded structure of GdIOP may be an effective strategy to achieve T_1-T_2 dual-modal contrasts through attenuating M_s (or T_2 interference effect) while without sacrificing T_2 effect.

To further investigate the relationships between embedded Gd_2O_3 clusters and the T_1 and T_2 relaxivities, we synthesized two other Gd-rich and Gd-poor GdIOP samples with similar sizes and surface structures but with Gd percentages of about 26.6 and 11.1%, respectively (Figure S6 in Supporting Information). The results show that the more Gd species in GdIOP, the higher r_1 and r_2 values are obtained. The Gd-poor and Gd-rich GdIOP samples exhibit r_1 of 46.7 ± 2.0 and 66.3 ± 3.1 mM^{-1} s^{-1} at 0.5 T, respectively (Table S1 in Supporting Information). The r_2 values are of 122.1 ± 7.9 and 215.7 ± 4.2 mM^{-1} s^{-1} at 0.5 T for Gd-poor and Gd-rich GdIOP, respectively. These results further imply that the synergistic effect of multiple iron oxide

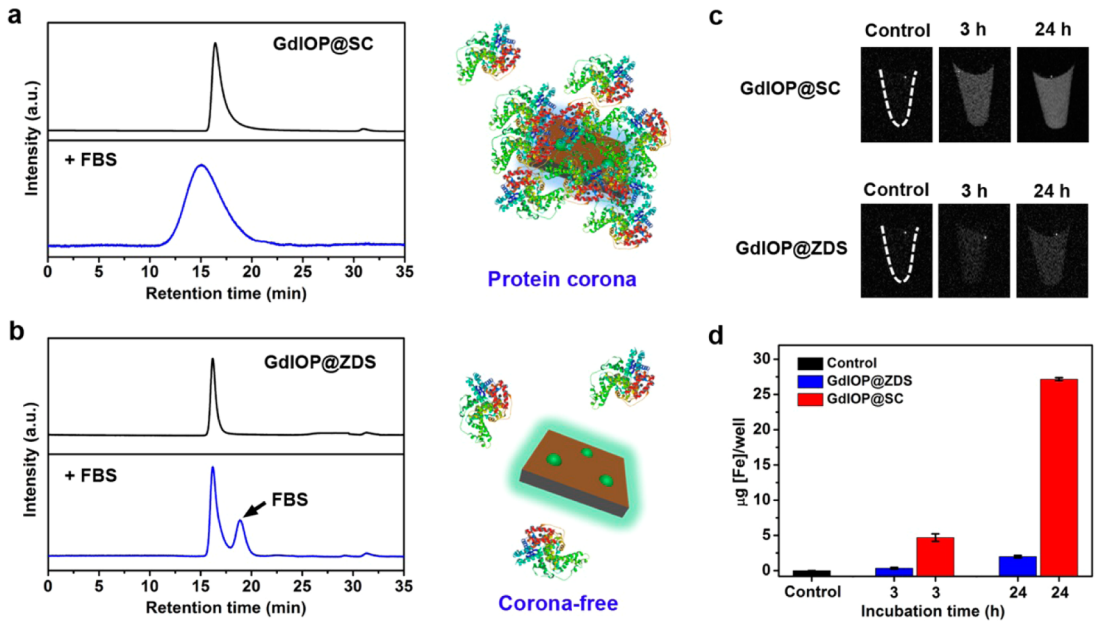

Figure 3. Engineering on nanobio interfacial property of GdIOPs. (a,b) HPLC-GFC profiles of GdIOP@SC and GdIOP@ZDS before (upper) and after (lower) incubated with 20% (v/v) FBS for 3 h. The retention time changes for GdIOP@SC indicate possibly formation of protein corona in the presence of serum proteins, whereas the peak of GdIOP@ZDS is clearly distinguishable from FBS in GFC profile probably owing to the corona-free characteristic. (c) T_1 MRI of SMCC-7721 cells after incubated with same concentrations of GdIOP@SC and GdIOP@ZDS samples for 3 and 24 h. Cells were collected and mixed with 50% (v/v) agarose gel. The brighter signals indicate enhanced cellular uptake of GdIOP@SC than that of GdIOP@ZDS. The control group was PBS for comparison. (d) Quantification of cellular uptake of GdIOP@SC and GdIOP@ZDS samples with about 5×10^6 cells per well (ICP analysis, $n = 3$. Data represent mean ± s.d.).

domains are major contributions to T_2 relaxation enhancement, while the high proportional of exposed Gd_2O_3 clusters are responsible for the enhanced T_1 effect because gadolinium ions are superior to iron ions in T_1 relaxation enhancement.

Nanobio Interfacial Property. Surface coating of nanoparticles plays a critical role in biomedical applications, which is relevant to biodistribution, toxicity, and clearance issues *in vivo*.[38,39] A thin layer coating on surface is also extremely important for nanoparticles as efficient T_1 MRI contrast agents.[25] We chose two small molecules sodium citrate (SC) and zwitterionic dopamine sulfonate (ZDS) as individual surface modifiers to achieve good water-dispersibility and water-permeability.[8] Zwitterion is an emerging platform that can avoid host nanoparticles from nonspecific adsorption with proteins, probably due to strong electostatic binding between zwitterion and water rather than weak hydrogen bonding.[40−42]

After ligand exchanging process, we used gel filtration chromatography (GFC) to determine the sizes of GdIOP@SC and GdIOP@ZDS because this method allows online analysis of nanoparticles with high reliability and repeatability.[43,44] The sizes of nanoparticles are inversely related to retention time incorporated with high performance liquid chromatography (HPLC) system. The GdIOP@SC and GdIOP@ZDS samples show a very similar retention time of 16.2 min in GFC profiles (Figure 3a,b, top), which are calibrated as about 12 nm using a series of protein standards (detailed in the Methods and in Figure S7 in Supporting Information). These results indicate that GdIOP is successfully coated with a thin layer on surface, which were also confirmed by TEM analysis (Figure S8 in Supporting Information). To further evaluate the potential stability *in vivo*, we monitored the size changes of GdIOP@SC and GdIOP@ZDS samples after incubated with 20% (v/v) fetal bovine serum (FBS) solution at 37 °C for 3 h. The GdIOP@SC appears an broadened peak with the retention time move forward to about 15.1 min, indicating the sizes grow to 30−50 nm (Figure 3a). This phenomenon may be ascribed to the formation of protein corona strucutures through nanspecific adsorption with serum proteins (Figure 3a, right). While the GdIOP@ZDS shows the stable retention time with a sharp peak separated from individual FBS particles (Figure 3b and Figure S7 in Supporting Information), indicating corona-free characteristic of GdIOP@ZDS in the presence of serum proteins (Figure 3b, right). The dynamic light scattering (DLS) analysis also showed that GdIOP@ZDS are stable in PBS buffer (1×, pH 7.4) either with or without FBS with a size of about 11.8 nm, while the GdIOP@SC in PBS buffer (1×, pH 7.4) showed an increased size of about 65 nm in the presence of FBS (Figure S9 in Supporting Information). We also used sodium dodecyl sulfate polyacrylamide gel electrophoresis (SDS-PAGE) to further determine the corona-free or protein corona characteristic of GdIOP@ZDS or GdIOP@SC after incubated with FBS. The gel showed clear proteins separated from GdIOP@SC group with

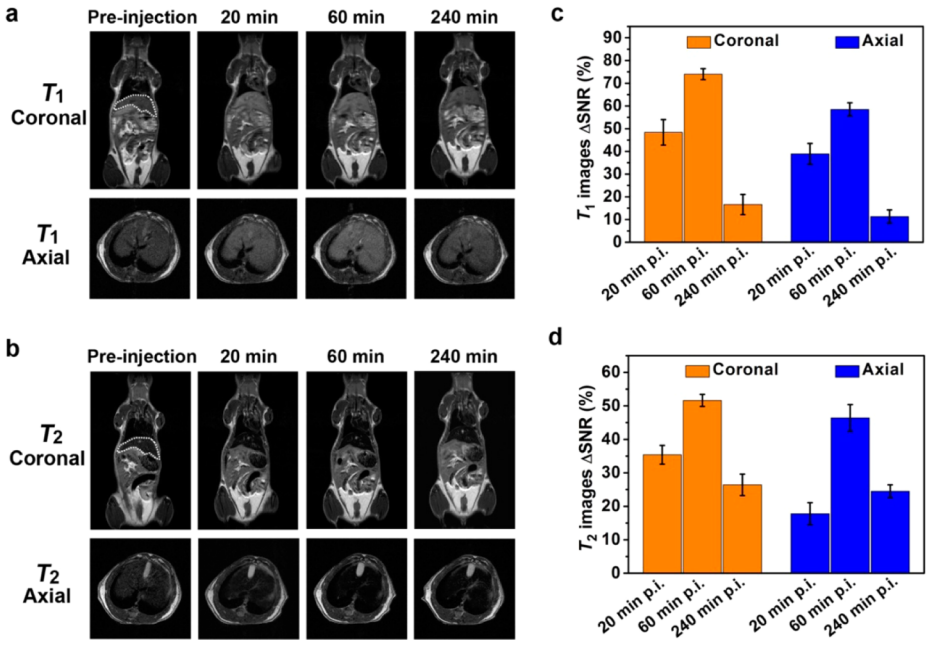

Figure 4. GdIOPs as T_1-T_2 dual-modal MRI contrast agents. (a) T_1- and T_2-weighted MR images (7.0 T) of mice acquired at preinjection and postinjection (p.i.) of GdIOP@SC with a dose of 2.0 mg (Fe + Gd)/kg mouse body weight. Each acquisition contains coronal and axial planes. The white dash circles in preinjection images indicate ROI of liver. Signal changes ΔSNR in liver of (c) T_1- and (d) T_2-weighted images at both coronal and axial planes (n = 3. Data represent mean ± s.d.), showing that maximal signal changes in liver were achieved at about 60 min p.i.

5 min, 1 and 3 h incubation time (Figure S10 in Supporting Information), indicating that the formation of protein corona happened within the first 5 min.[45,46] On the contrary, there were little observed proteins in gel for GdIOP@ZDS group under the same conditions, indicating a corona-free characteristic over a long period of time.

Accordingly, we then compared the cellular uptake efficiency of GdIOP@SC and GdIOP@ZDS samples using SMMC-7721 cell as an example. The cells were collected to conduct T_1 MRI after incubated with GdIOP@SC and GdIOP@ZDS samples (80 μg/mL). The GdIOP@SC treated cells show brighter contrasts in T_1 imaging than GdIOP@ZDS at both 3 and 24 h (Figure 3c), indicating that the formation of protein corona or agglomeration structure may enhance the cellular uptake efficiency (Figure S11 in Supporting Information). The ICP-MS analysis confirmed that cellular uptake of GdIOP@SC is about 14 folds higher than that of GdIOP@ZDS (Figure 3d). Meanwhile, 3-(4,5-dimethylthiazol-2-y1)-2,5-diphenyltetrazolium bromide (MTT) assay shows that GdIOP are nontoxic to both SMMC-7721 and Hela cells even at higher concentrations (120 μg/mL, Figure S12 in Supporting Information). It is noteworthy that cellular uptake of nanoparticles may vary between different shapes, surface coatings, and cell models.[47,48] Our results indicate that the formation of protein corona of GdIOP@SC may increase cognition of nanoaparticles by cells and enhance cellular uptake. Moreover, nanoparticles with protein corona strucuture in biofluids may be rapidly recognized by immune systems and accumulate in mononuclear phagocyte system (MPS),[27] which is of benefit to liver cancer diagnosis in clinic (*e.g.*, Feridex). On the contrary, nanoparticles with corona-free characteristic in biological fluids may escape from opsonization effect *in vivo*,[26,27] having great potential to control the nanobio interface and *in vivo* behaviors.

T_1-T_2 Dual-Modal MRI in Liver. We first used GdIOP@SC sample to evaluate the *in vivo* MRI performance at a 7.0 T MRI scanner. Because of potential formation of protein coronas in blood fluids, GdIOP@SC is prone to accumulate in liver owing to existence of a large number of hepatic Kuffer cells. T_1 and T_2 images at both coronal and transverse planes of region of interest (ROI) liver were acquired at preinjection and 20, 60, and 240 min postinjection (p.i.) of GdIOP@SC with a dose of 2.0 mg (Fe + Gd)/kg mouse body weight through tail vein. The ROIs at both planes reveal a brighter contrast in T_1 imaging and a darker contrast in T_2 imaging at 20 min after administration, suggesting rapid accumulation of GdIOP in liver (Figure 4a,b). Signal changes ΔSNR (signal-to-noise ratio, $\Delta SNR = |SNR_{post} - SNR_{pre}|/SNR_{pre}$) in ROI reached to maximum of 74.0% and 51.6% at about 60 min p.i. for T_1 and T_2 imaging, respectively (Figure 4c,d). Afterward, the ΔSNR dropped at 240 min p.i. may be due to excretion of GdIOP from liver into hepatobiliary metabolism pathway. These results indicate that GdIOP has potential to serve as a T_1-T_2 dual-modal MRI contrat agent for liver imaging, which may be helpful for accurate diagnosis of liver lesions.[10]

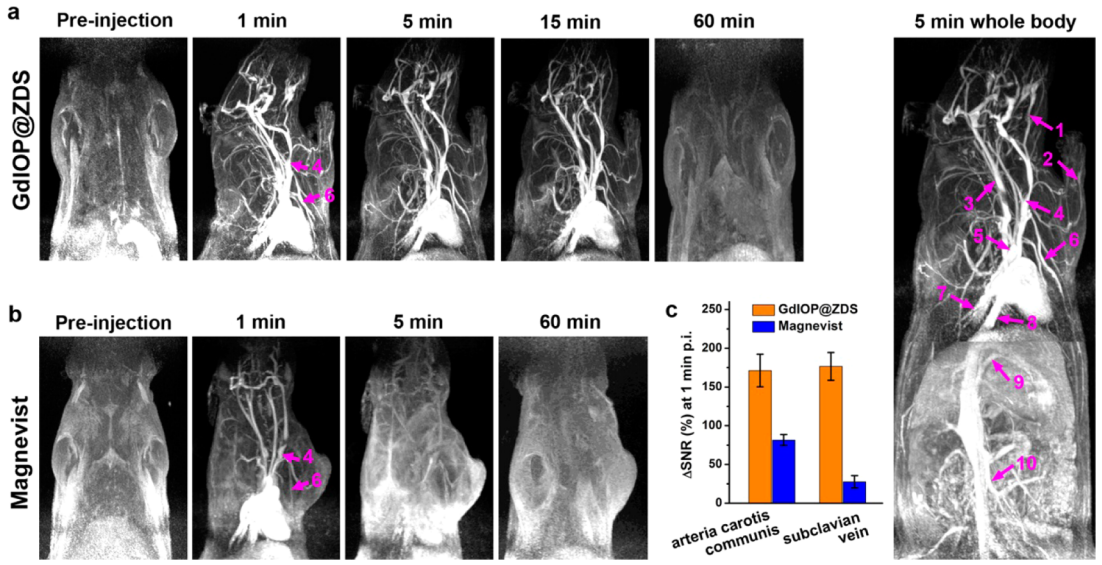

Figure 5. Contrast-enhanced MRA study at a clinical 3.0 T scanner. (a) MRA images of rats preinjection and postinjection (p.i.) of GdIOP@ZDS with a dose of 0.2 mmol (Fe + Gd)/kg rat body weight. At 5 min p.i., we acquired two scans in succession to show the whole body of rat. The labeled numbers in the images point out vascular details including: 1, inferior cerebral veins; 2, upper vein; 3, jugular vein; 4, arteria carotis communis; 5, arch of arota; 6, subclavian vein; 7, inferior vena cava; 8, descending aorta; 9, hepatic portal vein; and 10, rennal vein. (b) MRA study using a commercial contrast agent Magnevist (Gd-DTPA) with an injection dose of 0.2 mmol Gd/kg rat body weight, showing relatively low contrast enhancements in blood vessels and unavoidable perfusion of Gd into soft tissue space at 5 min p.i. (c) Comparison of quantification of signal changes ΔSNR at arteria carotis communis and subclavian vein after 1 min p.i. of GdIOP@ZDS or Magnevist (n = 3. Data represent mean ± s.d.).

Under the same conditions, we also evaluated MRI performance of Gd-rich GdIOP *in vivo*. The results show that T_2 contrast in mouse liver is evident, whereas T_1 contrast is barely found and turn to even darker at 120 and 240 min p.i. (Figure S13 in Supporting Information). This phenomenon can be attributed to the very strong T_2 decaying effect ($r_2 = 231.3 \pm 6.2$ mM^{-1} s^{-1} at 7.0 T) of Gd-rich GdIOP at transverse direction (Table S2 in Supporting Information), which may reduce T_1 signal recovery efficiency when longitudinal vectors turn to transverse plane.[1] At the mean time, we did the hematological and biochemical analysis and histological assessment of mice treated with GdIOP with a high dose of 5 mg (Fe + Gd)/kg mouse body weight (n = 3). The results show that major hematological parameters, liver function markers, and major organ tissues are normal in treatment groups comparing to controls (Figure S14 in Supporting Information), indicating good biocompatibility of GdIOP in the mouse model.

Contrast-Enhanced MRA Study. We then foused on the corona-free characteristic of GdIOP@ZDS as a potential MRA contrast agent. MRA is an important clinical tool to detect various blood diseases, such as myocardial infarction, atherosclerotic plaque, and tumor angiogenesis.[49−51] However, it is still challenging to achieve steady-state imaging and high-resolution contrast in MRA study using conventional molecular contrast agents, largely due to the relatively low efficacy and potentially redistribution of molecules into extracellular compartment.[19] GdIOP@ZDS takes advantages of highly efficient T_1 contrast ability and improved *in vivo* behaviors may hold great promise to serve as a novel MRA contrast agent.

We performed MRA study on rats (average body weight of 200 g) at a 3.0 T clinical scanner by intraveous injection of GdIOP@ZDS with a dose of 0.2 mmol (Fe + Gd)/kg rat body weight. Immediately, strong contrast in vascular nets was found at 1 min p.i. and the signal can maintain with superhigh resolution as long as 15 min (Figure 5a). At 5 min p.i., we acquired and merged two scans in sucession fouscing upper and lower part of rat body. The prominent vascular details of whole body inculding inferior cerebral veins, upper vein, jugular vein, arteria carotis communis, arch of arota, subclavian vein, inferior vena cava, descending aorta, hepatic portal vein, and rennal vein can be clearly distiguished (Figure 5a, and Supporting Video S1). More importantly, little signal intensity enhancement was found in interstitial space of rat body, indicating traceless perfusion of GdIOP into tissue space owing to an adequate nanometer size (*e.g.*, 7−12 nm).[19] On the contrary, a comparative study using the commercial T_1 contrast agent Magnevist (Gd-DTPA) shows weak contrast in vascular nets using the same dose of 0.2 mmol Gd/kg rat body weight (Figure 5b). An inherent reason is the relatively low r_1 value for Magnevist (~3.6 mM^{-1} s^{-1} at 3.0 T, Figure S15 in Supporting Information), which is about 5-fold lower than that of GdIOP. The ΔSNR values in arteria carotis communis and subclavian vein at one min p.i. of Magnevist are 2.1-fold and 6.5-fold lower than those of GdIOP, respectively (Figure 5c). The even lower ΔSNR

in subclavian vein may be attributed to immediate perfusion of molecular Magnevist into tissue space, which renders molecular Magnevist difficult to obtain detailed diagnostic information in veins by single injection. The perfusion effect for Magnevist became more obvious at about 5 min p.i., showing brighter signals spread throughout the rat body. In comparison with Magnevist, these results indicate that engineered GdIOP is a very superior MRA contrast agent with high-resolution in vascular details and an extended acquisition time window.

Although great efforts have been made to develop faster gradients, advanced pulse sequences, and novel k-space sampling strategies to meet the demands of faster acquisition speed for MRA, limits still exist on MRA study in terms of acquiring higher spatial resolution and contrast-to-noise ratio using conventional gadolinium chelating molecules.[52,53] Molecular contrast agents are prone to rapidly leak out from vascular nets during circulation due to ultrasmall size (<3 nm),[19] which causes the necessity for continual administrations of contrast agents during the finite imaging window of first pass MRA. Steady-state MRA enables increased signal-to-noise ratio and higher resolution by increasing the number of measurements and deactivation of partial k-space acquisition schemes. However, this technique requires longer and steady-state contrast window which is carefully executed considering the potential toxicity of gadolinium chelates. Gadolinium chelates were recently warned by U.S. Food and Drug Administration (FDA) with respect to its risk of causing nephrogenic systemic fibrosis (NSF), probably due to unexpected release of Gd ions by demetalation or transmetalation effect in physiological environment.[54] It is urgently needed to develop a highly efficient blood pool contrast agent toward to gain more precise diagnostic details in clinic applications. Nanoparticles with appropriate size and relatively good physiological stability are desirable as alternative solutions. More importantly, nanoparticles are prone to be modified on the chemical and physical properties, which allow us to modulate the MRI performance and *in vivo* behaviors of engineered nanoparticles.[20] The strategy of surface and interfacial engineering on magnetic nanoparticles is likely to become a new breakthrough to design highly efficient blood pool contrast agents, which may provide revolutionary alternations to molecular contrast agents in clinic.

CONCLUSIONS

In summary, we introduced an efficient strategy to develop high-performance MRI contrast agents through engineering on surface structure and nanobio interface. The enhanced T_1 and T_2 contrasts of GdIOP can be attributed to (i) the exposed metal centers on surface, and (ii) spin collection effect of the multidomain architectures. These features render GdIOP highly efficient in T_1 and T_2 contrast imaging, both *in vitro* and *in vivo*, in a wide scope of magnetic fields (0.5, 3.0, and 7.0 T). Moreover, we used ZDS as a surface modifier to adjust the nanobio interface of GdIOP, which shows highly efficient in MRA with excellent details in vascular nets and extended acquisition window. The merit of improved circulation time in blood fluids also holds great promise for GdIOP@ZDS to deliver guest drugs to tumor through enhanced permeation and retention effect. Overall, this study may shed light on the route to develop high-performance MRI contrast agents through engineering on surface and nanobio interface of magnetic nanoparticles for sensitive and accurate diagnosis in complex biological systems.

METHODS

Synthesis of GdIOP. The synthesis of GdIOP is straightforward as following: gadolinium oleate and iron oleate complex were prepared from reaction of sodium oleate and $GdCl_3$ and $FeCl_3$ with needed molar raitos. The obtained dry oleate complex (1 mmol) was dissolved in 1-octadecene (15 mL) with addition of oleci acid (0.16 mL) as surfactant. The reaction system was allowed to reflux in N_2 atomsphere for 2 h. After cooling to room temperature, excess isopropanol was added to the solution. The black products were collected by centrifugation and redispersed in hexane for further use.

X-ray Absorption Spectroscopy (XAS) Measurements. The Fe K-edge X-ray absorption spectra were recorded at beamline BL14W1 of Shanghai Synchrotron Radiation Facility (SSRF, at Shanghai, China) with the electron storage ring operated at 3.5 GeV. The Fe K-edge spectra of Fe foil standard was measured simultaneously at the third ionization chamber and was used for the energy calibration. The data was collected in the transmittance mode using Si(111) double-crystal monochromator. The as-obtained XAS data were processed according to the standard procedures using ATHENA software implemented in the IFEFFIT packages.

Preparation of Sodium Citrate (SC) or Zwitterionic Dopamine Sulfonate (ZDS) Coated GdIOP. The preparation of SC or ZDS coated GdIOP were carried out through a ligand exchange process. Excess of SC or ZDS (10 mg) were dissolved in 5 mL of ultrapure water and 10 mL of acetone, the as-prepared hexane-dispersed GdIOP (0.1 mmol) was added to the flask. The solution was then heated to reflux for 2 h before the nanoparticles were precipitated, suggesting the successful ligand exchange. The precipitation were then collected by centrifugation and redispered in distilled water. The final products were stored at 4 °C for further use.

MRI Relaxivity and MR Phantom Study. The GdIOP with various total metal (Fe and Gd) concentrations were prepared within 1% agar for MR phantom study. Longitudinal and transverse relaxation times were measured and used for calculating the relaxivities of GdIOP. T_2-weighted and T_1-weighted MR images were acquired at four different scanners under the following parameters: TR/TE = 2000/80 ms (T_2), TR/TE = 300/10 ms (T_1), 128 × 256 matrices, Repetition times = 8.

Cell Culture. All cell lines (HeLa and SMMC-7721) were purchased from Cell Bank of Chinese Academy of Sciences (Shanghai, China) and cultured in Dulbecco's Modified Eagle's Medium (DMEM medium with high glucose and 4.0 mM L-glutamine, no sodium pyruvate) supplemented with 10% fetal bovine serum (FBS, Hyclone). No antibiotic was added. All cells

were maintained in a humidified incubator at 37 °C with 5% CO_2.

Identification of Protein Corona or Corona-Free by SDS-PAGE. A total of 300 μL (10 μM) of GdIOP@SC or GdIOP@ZDS was added to 1 mL of diluted FBS in PBS solution to reach the final concentrations of 20% FBS (v/v), respectively. The solution were incubated at 37 °C for 5 min, 1 and 3 h, respectively, and the nanoparticles were isolated by centrifugation at 4 °C, 14 000 rpm for 20 min. After the removal of supernate, the residual nanoparticles were dissolved in 60 μL of loading buffer (62.5 mM Tris-HCl, 2% (w/v) SDS, 10% glycerol, 0.04 M dithiothreitol, and 0.01% (w/v) bromophenol blue) and heated for 10 min at 95 °C. Samples were loaded on acrylamide and run at stock gel (5%) for 10 min (90 V) and at separated gel (8%) for 60 min (130 V). The gel was then stained with Coomassie brilliant blue (CBB) and washed in diluted water.

Cytotoxicity Assay. The cytotoxicity of GdIOP was tested by MTT (3-(4,5-dimethylthiazol-2-y1)-2,5-diphenyltetrazolium bromide) method using HeLa and SMMC-7721 cells as models. Cells were first seeded into a 96-well plate with a density of 1×10^4 cells/well in DMEM at 37 °C, and incubated in the condition of 5% CO_2 for 24 h. Followed by addtion of different concentrations of GdIOP, each well was then added with 100 μL (0.5 mg/mL) of MTT and the plate was incubated for 4 h at 37 °C. After the addition of 100 μL of DMSO per well, the plate was kept at room temperature for 4 h. The OD_{490} values (Abs.) of each well were measured by a MultiSkan FC microplate reader. Cell viability was calculated from OD_{490} value of experimental group by subtracting that of blank group.

Hematology and Serum Biochemistry Analysis. Animal experiments were executed according to the protocol approved by Institutional Animal Care and Use Committee of Xiamen University. Before *in vivo* experiments, the samples were filtered through sterilized membrane filters (pore size 0.22 μm) to eliminate germs and stored in sterilized vials for use immediately. Female ICR mice were randomly separated as control group ($n = 3$) and experimental group ($n = 3$). Mice groups were then injected with PBS and GdIOP solution in the same volume (100 μL) through tail vein. The dose for experimental group is 5 mg/kg mouse body weight with respect to total metal ions. At 24 h postinjection, mice were sacrificed to collect blood immediately after confirmed death for hematology analysis and serum biochemistry analysis.

Gel Filtration Chromatography (GFC). We performed the GFC analysis on a Superdex-75 10/300 GL column (GE Healthcare Life Sciences) in a high performance liquid chromatography (HPLC) (UltiMate 3000, Dionex) system. The mobile phase is PBS buffer (1×, pH 7.4) with the flow rate as 0.5 mL/min. The protein standards with known hydrodynamic diameter containing blue dextran (2000 kDa, 29.5 nm HD), alcohol dehydrogenase (150 kDa, 10.1 nm HD), ovalbumin (44 kDa, 6.13 nm HD), and vitamin B_{12} (1.35 kDa, 1.5 nm HD), denoted as M1-M4, were used for calibrating the size of samples. The serum binding test were performed by mixing 1 μM of nanoparticles and 20% (v/v) FBS and incubating for 3 h at 37 °C before to run HPLC under the same conditions. All standards and samples were tested in triplicate.

Magnetic Resonance Angiography (MRA) Study. MRA was performed on a 3.0 T clinical scanner (Philips Medical System, ACHIEVA 3.0 T) using a rat coil to acquire signals. Sprague−Dawley (SD) Rats (200 g) were anaesthetized by pentobarbital sodium at a dose of 40 mg/kg body weight under the protocol approved by Institutional Animal Care and Use Committee. T_1-weighted images were obtained at pre- and postinjection of GdIOP@ZDS or Magnevist (control) with a dose of 0.2 mmol metal ions/kg body weight through tail vein. Dynamic MRA images were acquired using 3D-CEMRA sequence with parameters as follows: T_1-weighted fast field echo (T1FFE), TR = 7 ms, TE = 3 ms, field of view (FOV) = 100 mm × 100 mm, slices = 60, slice thickness = 1 mm, Flip angle = 30°.

Conflict of Interest: The authors declare no competing financial interest.

Acknowledgment. This work was supported by the National Key Basic Research Program of China (2013CB933900, 2014CB744502 and 2014CB932004), National Natural Science Foundation of China (21222106, 81370042 and 81430041), Natural Science Foundation of Fujian (2013J06005), IRT13036, and Fok Ying Tung Education Foundation (142012). The authors thank Profs. G. Liang, W. Chu and P. Zhang for XAS measurements and fruitful discussions.

Supporting Information Available: The XPS analysis, TEM images, XRD pattern, M-T curves, DLS, MTT assay, H&E staining, and an additional 3D rotational MRA video. This material is available free of charge *via* the Internet at http://pubs.acs.org.

REFERENCES AND NOTES

1. Liang, Z. P.; Lauterbur, P. C. *Principles of Magnetic Resonance Imaging: A Signal Processing Perspective*. Wiley-IEEE Press: New York, 1999.
2. Ananta, J. S.; Godin, B.; Sethi, R.; Moriggi, L.; Liu, X.; Serda, R. E.; Krishnamurthy, R.; Muthupillai, R.; Bolskar, R. D.; Helm, L.; *et al.* Geometrical Confinement of Gadolinium-Based Contrast Agents in Nanoporous Particles Enhances T_1 Contrast. *Nat. Nanotechnol.* **2010**, *5*, 815–821.
3. Major, J. L.; Meade, T. J. Bioresponsive, Cell-Penetrating, and Multimeric MR Contrast Agents. *Acc. Chem. Res.* **2009**, *42*, 893–903.
4. Laurent, S.; Forge, D.; Port, M.; Roch, A.; Robic, C.; Vander Elst, L.; Muller, R. N. Magnetic Iron Oxide Nanoparticles: Synthesis, Stabilization, Vectorization, Physicochemical Characterizations, and Biological Applications. *Chem. Rev.* **2008**, *108*, 2064–2110.
5. Reddy, L. H.; Arias, J. L.; Nicolas, J.; Couvreur, P. Magnetic Nanoparticles: Design and Characterization, Toxicity and Biocompatibility, Pharmaceutical and Biomedical Applications. *Chem. Rev.* **2012**, *112*, 5818–5878.
6. Lee, N.; Hyeon, T. Designed Synthesis of Uniformly Sized Iron Oxide Nanoparticles for Efficient Magnetic Resonance Imaging Contrast Agents. *Chem. Soc. Rev.* **2012**, *41*, 2575.
7. Kim, B. H.; Lee, N.; Kim, H.; An, K.; Park, Y. I.; Choi, Y.; Shin, K.; Lee, Y.; Kwon, S. G.; Na, H. B.; *et al.* Large-Scale Synthesis of Uniform and Extremely Small-Sized Iron Oxide Nanoparticles for High-Resolution T_1 Magnetic Resonance Imaging Contrast Agents. *J. Am. Chem. Soc.* **2011**, *133*, 12624–12631.
8. Zhou, Z. J.; Wang, L. R.; Chi, X.; Bao, J. F.; Yang, L.; Zhao, W.; Chen, Z.; Wang, X.; Chen, X. Y.; Gao, J. H. Engineered Iron-Oxide-Based Nanoparticles as Enhanced T_1 Contrast Agents for Efficient Tumor Imaging. *ACS Nano* **2013**, *7*, 3287–3296.
9. Huang, G.; Li, H.; Chen, J.; Zhao, Z.; Yang, L.; Chi, X.; Chen, Z.; Wang, X.; Gao, J. Tunable T_1 and T_2 Contrast Abilities of Manganese-Engineered Iron Oxide Nanoparticles Through Size Control. *Nanoscale* **2014**, *6*, 10404–10412.
10. Zhou, Z. J.; Huang, D. T.; Bao, J. F.; Chen, Q. L.; Liu, G.; Chen, Z.; Chen, X. Y.; Gao, J. H. A Synergistically Enhanced T_1-T_2 Dual-Modal Contrast Agent. *Adv. Mater.* **2012**, *24*, 6223–6228.
11. Lee, J. H.; Huh, Y. M.; Jun, Y. w.; Seo, J.-w.; Jang, J.-t.; Song, H.-T.; Kim, S.; Cho, E.-J.; Yoon, H.-G.; Suh, J.-S.; *et al.* Artificially Engineered Magnetic Nanoparticles for Ultra-Sensitive Molecular Imaging. *Nat. Med.* **2006**, *13*, 95–99.
12. Huang, G.; Hu, J.; Zhang, H.; Zhou, Z.; Chi, X.; Gao, J. Highly Magnetic Iron Carbide Nanoparticles as Effective T_2 Contrast Agents. *Nanoscale* **2014**, *6*, 726–730.
13. Zhao, Z. H.; Zhou, Z. J.; Bao, J.; Wang, Z.; Hu, J.; Chi, X.; Ni, K.; Wang, R.; Chen, X.; Chen, Z.; *et al.* Octapod Iron Oxide Nanoparticles as High-Performance T_2 Contrast Agents for Magnetic Resonance Imaging. *Nat. Commun.* **2013**, *4*, 2266.
14. Lee, N.; Kim, H.; Choi, S. H.; Park, M.; Kim, D.; Kim, H. C.; Choi, Y.; Lin, S.; Kim, B. H.; Jung, H. S.; *et al.* Magnetosome-Like Ferrimagnetic Iron Oxide Nanocubes for Highly Sensitive MRI of Single Cells and Transplanted Pancreatic Islets. *Proc. Natl. Acad. Sci. U. S. A.* **2011**, *108*, 2662–2667.
15. Lee, N.; Choi, Y.; Lee, Y.; Park, M.; Moon, W. K.; Choi, S. H.; Hyeon, T. Water-Dispersible Ferrimagnetic Iron Oxide

Nanocubes with Extremely High r_2 Relaxivity for Highly Sensitive *In Vivo* MRI of Tumors. *Nano Lett.* **2012**, *12*, 3127–3131.
16. Kim, W. Y.; Danias, P. G.; Stuber, M.; Flamm, S. D.; Plein, S.; Nagel, E.; Langerak, S. E.; Weber, O. M.; Pedersen, E. M.; Schmidt, M.; *et al.* Coronary Magnetic Resonance Angiography for the Detection of Coronary Stenoses. *New Engl. J. Med.* **2001**, *345*, 1863–1869.
17. Oudkerk, M.; van Beek, E. J. R.; Wielopolski, P.; van Ooijen, P. M. A.; Brouwers-Kuyper, E. M. J.; Bongaerts, A. H. H.; Berghout, A. Comparison of Contrast-Enhanced Magnetic Resonance Angiography and Conventional Pulmonary Angiography for the Diagnosis of Pulmonary Embolism: A Prospective Study. *Lancet* **2002**, *359*, 1643–1647.
18. Zhang, H.; Maki, J. H.; Prince, M. R. 3D Contrast-Enhanced MR Angiography. *J. Magn. Reson. Imaging* **2007**, *25*, 13–25.
19. Kobayashi, H.; Brechbiel, M. W. Nano-Sized MRI Contrast Agents with Dendrimer Cores. *Adv. Drug Delivery Rev.* **2005**, *57*, 2271–2286.
20. Li, C. A Targeted Approach to Cancer Imaging and Therapy. *Nat. Mater.* **2014**, *13*, 110–115.
21. Marckmann, P.; Skov, L.; Rossen, K.; Dupont, A.; Damholt, M. B.; Heaf, J. G.; Thomsen, H. S. Nephrogenic Systemic Fibrosis: Suspected Causative Role of Gadodiamide Used for Contrast-Enhanced Magnetic Resonance Imaging. *J. Am. Soc. Nephrol.* **2006**, *17*, 2359–2362.
22. Brisman, J. L.; Song, J. K.; Newell, D. W. Medical Progress: Cerebral Aneurysms. *New Engl. J. Med.* **2006**, *355*, 928–939.
23. Nel, A. E.; Madler, L.; Velegol, D.; Xia, T.; Hoek, E. M. V.; Somasundaran, P.; Klaessig, F.; Castranova, V.; Thompson, M. Understanding Biophysicochemical Interactions at the Nano-Bio Interface. *Nat. Mater.* **2009**, *8*, 543–557.
24. Pelaz, B.; Jaber, S.; de Aberasturi, D. J.; Wulf, V.; Aida, T.; de la Fuente, J. M.; Feldmann, J.; Gaub, H. E.; Josephson, L.; Kagan, C. R.; *et al.* The State of Nanoparticle-Based Nanoscience and Biotechnology: Progress, Promises, and Challenges. *ACS Nano* **2012**, *6*, 8468–8483.
25. Zhou, Z. J.; Zhao, Z. H.; Zhang, H.; Wang, Z.; Chen, X.; Wang, R.; Chen, Z.; Gao, J. Interplay between Longitudinal and Transverse Contrasts in Fe_3O_4 Nanoplates with (111) Exposed Surfaces. *ACS Nano* **2014**, *8*, 7976–7985.
26. Walkey, C. D.; Chan, W. C. W. Understanding and Controlling the Interaction of Nanomaterials with Proteins in a Physiological Environment. *Chem. Soc. Rev.* **2012**, *41*, 2780–2799.
27. Monopoli, M. P.; Åberg, C.; Salvati, A.; Dawson, K. A. Biomolecular Coronas Provide the Biological Identity of Nanosized Materials. *Nat. Nanotechnol.* **2012**, *7*, 779–786.
28. Wu, Z. S.; Yang, S.; Sun, Y.; Parvez, K.; Feng, X.; Müllen, K. 3D Nitrogen-Doped Graphene Aerogel-Supported Fe_3O_4 Nanoparticles as Efficient Electrocatalysts for the Oxygen Reduction Reaction. *J. Am. Chem. Soc.* **2012**, *134*, 9082–9085.
29. Chen, W.; Li, S.; Chen, C.; Yan, L. Self-Assembly and Embedding of Nanoparticles by *In Situ* Deduced Graphene for Preparation of a 3D Graphene/Nanoparticle Aerogel. *Adv. Mater.* **2011**, *23*, 5679–5683.
30. Westre, T. E.; Kennepohl, P.; DeWitt, J. G.; Hedman, B.; Hodgson, K. O.; Solomon, E. I. A Multiplet Analysis of Fe K-Edge 1s→3d Pre-Edge Features of Iron Complexes. *J. Am. Chem. Soc.* **1997**, *119*, 6297–6314.
31. Zając, D. A.; Woch, W. M.; Stępień, J.; Kapusta, C.; Kołodziejczyk, A.; Sudra, H.; Gritzner, G. XANES and EXAFS Study of $(Tl_{0.5}Pb_{0.5})Sr_2(Ca_{1-x}Gd_x)Cu_2Oz$ Superconductors. *Radiat. Phys. Chem.* **2013**, *93*, 33–36.
32. Merte, L. R.; Peng, G.; Bechstein, R.; Rieboldt, F.; Farberow, C. A.; Grabow, L. C.; Kudernatsch, W.; Wendt, S.; Lægsgaard, E.; Mavrikakis, M.; *et al.* Water-Mediated Proton Hopping on an Iron Oxide Surface. *Science* **2012**, *336*, 889–893.
33. Sun, X.; Kurahashi, M.; Pratt, A.; Yamauchi, Y. First-Principles Study of Atomic Hydrogen Adsorption on Fe_3O_4(100). *Surf. Sci.* **2011**, *605*, 1067–1073.
34. Hwang, L. P.; Freed, J. H. Dynamic Effects of Pair Correlation Functions on Spin Relaxation by Translational Diffusion in Liquids. *J. Chem. Phys.* **1975**, *63*, 4017–4025.
35. Gillis, P.; Koenig, S. H. Transverse Relaxation of Solvent Protons Induced by Magnetized Spheres: Application to Ferritin, Erythrocytes, and Magnetite. *Magn. Reson. Med.* **1987**, *5*, 323–345.
36. Ai, H.; Flask, C.; Weinberg, B.; Shuai, X. T.; Pagel, M. D.; Farrell, D.; Duerk, J.; Gao, J. Magnetite-Loaded Polymeric Micelles as Ultrasensitive Magnetic-Resonance Probes. *Adv. Mater.* **2005**, *17*, 1949–1952.
37. Taktak, S.; Sosnovik, D.; Cima, M. J.; Weissleder, R.; Josephson, L. Multiparameter Magnetic Relaxation Switch Assays. *Anal. Chem.* **2007**, *79*, 8863–8869.
38. Khlebtsov, N.; Dykman, L. Biodistribution and Toxicity of Engineered Gold Nanoparticles: A Review of *In Vitro* and *In Vivo* Studies. *Chem. Soc. Rev.* **2011**, *40*, 1647–1671.
39. Liu, G.; Gao, J.; Ai, H.; Chen, X. Applications and Potential Toxicity of Magnetic Iron Oxide Nanoparticles. *Small* **2013**, *9*, 1533–1545.
40. Keefe, A. J.; Jiang, S. Poly(zwitterionic)protein Conjugates Offer Increased Stability without Sacrificing Binding Affinity or Bioactivity. *Nat. Chem.* **2012**, *4*, 59–63.
41. Moyano, D. F.; Saha, K.; Prakash, G.; Yan, B.; Kong, H.; Yazdani, M.; Rotello, V. M. Fabrication of Corona-Free Nanoparticles with Tunable Hydrophobicity. *ACS Nano* **2014**, *8*, 6748–6755.
42. Cao, Z.; Jiang, S. Super-Hydrophilic Zwitterionic Poly(carboxybetaine) and Amphiphilic Non-Ionic Poly(ethylene glycol) for Stealth Nanoparticles. *Nano Today* **2012**, *7*, 404–413.
43. Choi, H. S.; Liu, W.; Liu, F.; Nasr, K.; Misra, P.; Bawendi, M. G.; Frangioni, J. V. Design Considerations for Tumour-Targeted Nanoparticles. *Nat. Nanotechnol.* **2010**, *5*, 42–47.
44. Choi, H. S.; Liu, W.; Misra, P.; Tanaka, E.; Zimmer, J. P.; Itty Ipe, B.; Bawendi, M. G.; Frangioni, J. V. Renal Clearance of Quantum Dots. *Nat. Biotechnol.* **2007**, *25*, 1165–1170.
45. Walczyk, D.; Bombelli, F. B.; Monopoli, M. P.; Lynch, I.; Dawson, K. A. What the Cell "Sees" in Bionanoscience. *J. Am. Chem. Soc.* **2010**, *132*, 5761–5768.
46. Jedlovszky-Hajdú, A.; Bombelli, F. B.; Monopoli, M. P.; Tombácz, E.; Dawson, K. A. Surface Coatings Shape the Protein Corona of SPIONs with Relevance to Their Application *In Vivo*. *Langmuir* **2012**, *28*, 14983–14991.
47. Walkey, C. D.; Olsen, J. B.; Guo, H.; Emili, A.; Chan, W. C. W. Nanoparticle Size and Surface Chemistry Determine Serum Protein Adsorption and Macrophage Uptake. *J. Am. Chem. Soc.* **2011**, *134*, 2139–2147.
48. Huang, J.; Bu, L.; Xie, J.; Chen, K.; Cheng, Z.; Li, X.; Chen, X. Effects of Nanoparticle Size on Cellular Uptake and Liver MRI with Polyvinylpyrrolidone-Coated Iron Oxide Nanoparticles. *ACS Nano* **2010**, *4*, 7151–7160.
49. Allkemper, T.; Bremer, C.; Matuszewski, L.; Ebert, W.; Reimer, P. Contrast-Enhanced Blood-Pool MR Angiography with Optimized Iron Oxides: Effect of Size and Dose on Vascular Contrast Enhancement in Rabbits. *Radiology* **2002**, *223*, 432–438.
50. Tombach, B.; Reimer, P.; Bremer, C.; Allkemper, T.; Engelhardt, M.; Mahler, M.; Ebert, W.; Heindel, W. First-Pass and Equilibrium-MRA of the Aortoiliac Region with a Superparamagnetic Iron Oxide Blood Pool MR Contrast Agent (SH U 555 C): Results of a Human Pilot Study. *NMR Biomed.* **2004**, *17*, 500–506.
51. Yancy, A. D.; Olzinski, A. R.; Hu, T. C. C.; Lenhard, S. C.; Aravindhan, K.; Gruver, S. M.; Jacobs, P. M.; Willette, R. N.; Jucker, B. M. Differential Uptake of Ferumoxtran-10 and Ferumoxytol, Ultrasmall Superparamagnetic Iron Oxide Contrast Agents in Rabbit: Critical Determinants of Atherosclerotic Plaque Labeling. *J. Magn. Reson. Imaging* **2005**, *21*, 432–442.
52. Nikolaou, K.; Kramer, H.; Grosse, C.; Clevert, D.; Dietrich, O.; Hartmann, M.; Chamberlin, P.; Assmann, S.; Reiser, M. F.; Schoenberg, S. O. High-Spatial-Resolution Multistation MR Angiography with Parallel Imaging and Blood Pool Contrast Agent: Initial Experience. *Radiology* **2006**, *241*, 861–872.
53. Maki, J. H.; Wilson, G. J.; Eubank, W. B.; Glickerman, D. J.; Pipavath, S.; Hoogeveen, R. M. Steady-State Free Precession

MRA of the Renal Arteries: Breath-Hold and Navigator-Gated Techniques *vs* CE-MRA. *J. Magn. Reson. Imaging* **2007**, *26*, 966–973.
54. Penfield, J. G.; Reilly, R. F. What Nephrologists Need to Know about Gadolinium. *Nat. Clin. Pract. Nephrol.* **2007**, *3*, 654–668.